



Synthesis and Lithiation Mechanisms of Dirutile and Rutile LiMnF_4 : Two New Conversion Cathode Materials

Nancy Twu,* Xin Li, Charles Moore, and Gerbrand Ceder**z

Department of Materials Science and Engineering, Massachusetts Institute of Technology, Cambridge, Massachusetts 02139, USA

Driven by the need for new cathode battery materials with high energy density, fluorides have emerged as promising candidates due to their high voltages. From high throughput computations, dirutile LiMnF_4 was identified as a promising cathode with a high conversion voltage and a theoretical specific capacity of 584 mAh/g. In this work, we study the formation of dirutile LiMnF_4 through a new, low-temperature synthesis route and report its electrochemical properties. We also report the discovery of a new rutile polymorph of LiMnF_4 which has Li-Mn disorder on the cation site. Electron diffraction confirmed both dirutile and rutile LiMnF_4 to convert upon lithiation with different reaction paths. As seen with other fluoride materials, specific capacity is strongly linked with synthesis and processing conditions. With LiMnF_4 , there was a tradeoff in maintaining phase-pure samples and optimizing samples for high specific capacity. Still, even with very simple synthesis and electrode preparation methods, both rutile and dirutile polymorphs of LiMnF_4 show electrochemical activity. Further optimization of particle morphology may enhance reaction kinetics and improve specific capacity.

© 2013 The Electrochemical Society. [DOI: 10.1149/2.022311jes] All rights reserved.

Manuscript submitted June 21, 2013; revised manuscript received July 29, 2013. Published September 13, 2013.

Rechargeable lithium-ion batteries rely on the reversible, topotactic exchange of lithium ions between two host structures to store energy. While lithium-ion systems have found commercial success in portable electronics and have entered the electric vehicle market, their energy density is limited by the number of lithium ions transferrable between the two electrodes. Few intercalation cathodes can reversibly intercalate more than one lithium ion per formula unit before inducing decomposition reactions. This limits the specific capacity and resulting energy density of a lithium-ion battery.

Conversion cathode materials offer one path forward in achieving much higher energy densities than traditional lithium-ion batteries.¹⁻³ In conversion reactions, multiple lithium atoms react with the cathode to utilize all the redox states of the transition metal. The host structure is not conserved; instead, it converts to a multitude of other phases upon lithiation. Of the conversion cathode materials considered to date, fluorides are the most attractive due to their high voltage, which derives from the ionic nature of the metal-fluorine bond. Using simple electrode preparation techniques, Arai et al. gave the first report of the electrochemical activity of the binary metal fluorides FeF_3 , TiF_3 , VF_3 , and MnF_3 .⁴ Despite having high theoretical specific capacities of >200 mAh/g with one lithium, only 80 mAh/g could be reversibly cycled in the former three compounds, and no discharge capacity was observed for MnF_3 . This illustrates one of the main challenges in fluoride systems: while the electronegativity of fluorine gives rise to high voltages, fluorides also tend to be insulators.

Badway et al. later demonstrated a means of compensating for the inherently low conductivity of fluoride cathodes. By aggressively mixing FeF_3 with carbon to obtain sub-30 nm particles and form carbon metal fluoride nanocomposites, much higher capacities could be realized.^{2,5} FeF_3 reached a specific capacity of 200 mAh/g at a 2 V cutoff by accessing the $\text{Fe}^{3+}/\text{Fe}^{2+}$ redox couple, and >600 mAh/g at a 1.5 V cutoff when further reducing Fe^{2+} to Fe^0 . The high specific capacity achieved in the FeF_3 system prompted a series of studies on other metal fluoride and oxyfluoride systems, including FeF_2 ,⁶⁻⁸ FeOF ,^{9,10} CuF_2 ,^{7,11} BiOF_3 and BiF_3 .¹² Research efforts on conversion materials include optimization of particle morphology for improved performance,¹³ as well as elucidation of reaction paths through computation^{14,15} and in situ TEM studies.^{7,8} Despite successes in these efforts, there continues to be a need for new, high energy density materials. Computations have been shown to be effective both in identifying promising new materials and supporting experimental observation.^{16,17}

One such new material is dirutile LiMnF_4 , which is monoclinic with space group $\text{P2}_1/c$ and unit cell parameters of $a = 5.41 \text{ \AA}$, $b = 4.63 \text{ \AA}$, $c = 5.69 \text{ \AA}$, and $\beta = 113.24^\circ$. As described by Laccorre et al.,¹⁸ the dirutile structure has twice the periodicity of a true rutile due to ordering of planes of Li^+ and Mn^{3+} ions in the [100] direction (Figure 1a). Along the [101] direction, edge-sharing LiF_6 and MnF_6 octahedra alternate to form a rutile-like structure with empty channels between edge-sharing octahedral chains (Figure 1b).

Dirutile LiMnF_4 was computationally identified¹⁹ as a promising conversion cathode with high reaction voltages and a theoretical specific capacity of 583 mAh/g upon full conversion. This specific capacity is comparable to rutile FeF_2 , one of the most promising conversion materials studied to date. Our computations also suggested that insertion to Li_2MnF_4 was plausible, even if not the equilibrium reaction. In this work, we synthesized dirutile LiMnF_4 via a new low-temperature mechanochemical/solid state route, and discovered a new metastable rutile polymorph of LiMnF_4 . Both rutile and dirutile phases were tested and shown to be electrochemically active. TEM electron diffraction on discharged samples confirmed lithiation of both phases of LiMnF_4 to occur via conversion reactions, but not necessarily via the equilibrium path. Computations were used to analyze energetics of different reaction pathways and provide supporting theory to experimental observations.

Methods

Computational methods.— All computations were performed using density functional theory (DFT) using the generalized gradient approximation with a Hubbard-like U correction (GGA+U).^{20,21} The U value for the d states of Mn was set to 3.9 eV as determined by fitting experimental oxidation energies.¹⁹ The Vienna ab initio Simulation Package (VASP) and the included projector-augmented pseudopotentials were used for all calculations. All calculations were performed with ferromagnetic spin alignment. The calculated Li-Mn-F phase diagram, the expected conversion products, and their associated energies and voltages were obtained from the Materials Project.^{19,22}

Synthesis methods.— Stoichiometric amounts of LiF (99.99% Alfa Aesar Puratronic) and MnF_3 (99.9%, Sigma Aldrich) were milled together in a Retsch PM200 planetary ball mill for 6 hours at 500 rpm, with up to 10% excess MnF_3 . Ball mill jars were assembled and re-opened in an argon-filled glovebox to prevent exposure to air and moisture throughout sample processing. Heating the milled precursors in a tube furnace under argon between 300–600°C for 10 hours produced the dirutile LiMnF_4 phase. Additional milling of dirutile

*Electrochemical Society Student Member.

**Electrochemical Society Active Member.

zE-mail: g.ceder@mit.edu

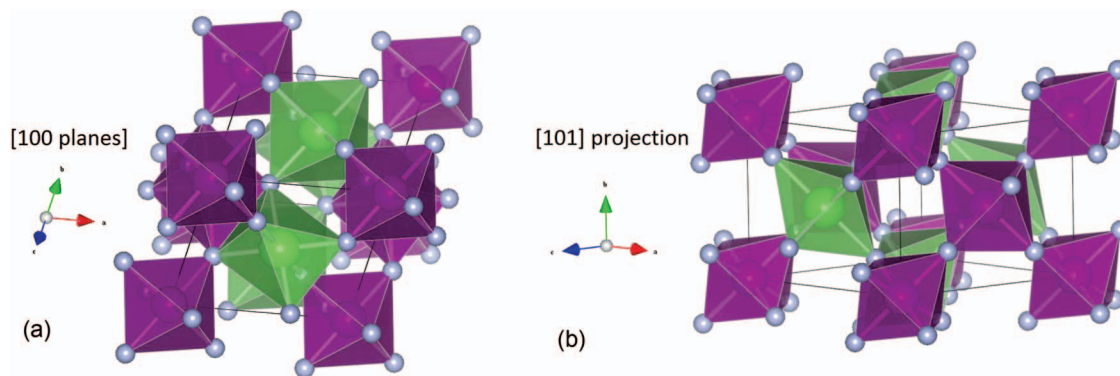


Figure 1. (a) Dirutile LiMnF_4 has [100] planes of corner-sharing octahedral of a single cation species. (b) The projection of dirutile LiMnF_4 along [101] shows empty channels formed between the edge-sharing octahedral chains.

LiMnF_4 for 6–12 hours at 500 rpm in a planetary ball mill formed the new rutile LiMnF_4 phase.

Characterization.— The X-ray diffraction (XRD) patterns in Figure 2 and Supplemental Figure 2 were collected on a Rigaku RU300 Cr-source diffractometer with step scans between $10\text{--}120^\circ 2\theta$, and the XRD patterns in Figure 3 and Figure 5 were collected on a Bruker D8 Advance Da Vinci Mo-source diffractometer with step scans between $5\text{--}30^\circ 2\theta$. These patterns are all converted to the 2θ range corresponding to a Cu XRD source for this paper. All samples were sealed with Kapton film to avoid air exposure. Powder diffraction data in Figure 4 was collected in capillaries at Brookhaven National Laboratory NSLS, beamline x14A ($\lambda = 7.75756 \text{ \AA}$). Rietveld refinement and profile matching of the powder diffraction data were performed using PANalytical High Score Plus.

TEM samples were prepared in an argon filled glovebox with both the O_2 and H_2O levels lower than 0.1 ppm. TEM samples of pristine rutile and dirutile LiMnF_4 powder were prepared by the dry method to minimize artifacts. The TEM samples for the pristine and discharged cathode films were prepared by a gentle sonication process in anhydrous dimethyl carbonate (DMC) with 20ppm H_2O . TEM samples were sealed in an airtight bottle in the glovebox and then transferred into the TEM vacuum column immediately after the sample bottle was opened. Approximately 30 Selected Area Electron Diffraction

(SAED) patterns for each type of sample were obtained from a JEOL 2010F Transmission Electron Microscope and indexed with PolyCrystalline Electron Diffraction Pattern (PCED2.0).

Electrochemistry.— To maintain single phase samples of dirutile or rutile LiMnF_4 , the active compound was milled with carbon black (super P) in a Retsch PM200 planetary ball mill for 2 hours at 500 rpm. XRD confirmed no dirutile-to-rutile phase transitions to occur after the two hour milling cycle with carbon. A two-phase sample of dirutile and rutile LiMnF_4 was obtained by milling dirutile LiMnF_4 for 12 hours at 500 rpm with carbon. All milling was performed under inert atmosphere by assembling and reopening ball mill jars in an argon-filled glovebox. The mixture of active material and carbon was then hand-mixed with polyethylenetetrafluoride (PTFE) binder in a ratio of 45:45:10 by weight, and rolled into a film. Swagelok cells were assembled in an argon-filled glovebox using lithium metal, Celgard C480 separator, and 1M LiPF_6 in 1:1 ethylene carbonate:dimethyl carbonate (EC:DMC) solution. Cells were also tested using 1M LiClO_4 in propylene carbonate (PC) as an alternative electrolyte, given the observations of fluoride instability in the presence of trace amounts of HF from LiPF_6 dissolution.²⁴ No noticeable differences in electrochemical performance were observed between the LiMnF_4 cells tested with different electrolytes. All cells were tested on a Maccor 2200 or Maccor 4000 operating at room temperature.

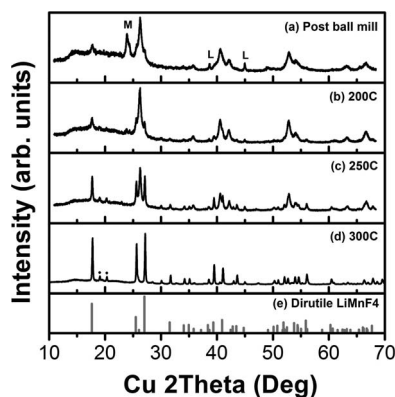


Figure 2. XRD reveals the formation of rutile LiMnF_4 by mechanochemical reaction, and transformation of rutile LiMnF_4 to dirutile LiMnF_4 by solid state reaction. XRD patterns are shown for (a) Ball milled LiF and MnF_3 . M = MnF_3 and L = LiF still unreacted after milling. (b) After heating the ball milled precursors to 200°C for 10 hr under argon. (c) After heating the ball milled precursors to 250°C for 10 hr under argon. (d) After heating the ball milled precursors to 300°C for 10 hr under argon. Black circles denote the main peaks of an impurity phase, Li_2MnF_5 . (e) Theoretical peak positions of dirutile LiMnF_4 , space group $\text{P2}_1/\text{c}$.

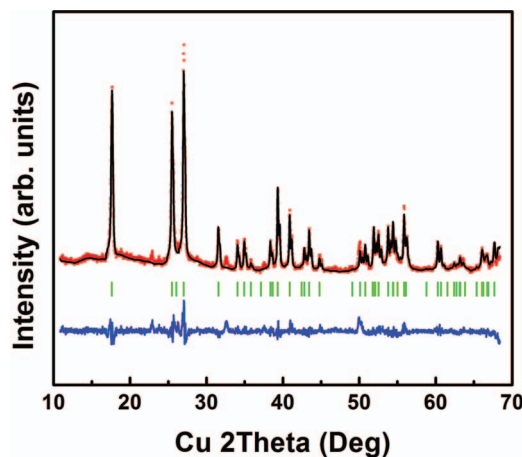


Figure 3. Rietveld refinement of dirutile LiMnF_4 on the $\text{P2}_1/\text{c}$ space group shows good agreement between the experimental (red) and refined (black) diffraction patterns with $R_{wp} = 12.3\%$ and $\text{GOF} = 3.336$. The peak positions for dirutile LiMnF_4 are shown by the green vertical lines, and the difference plot is shown by the bottom blue line.

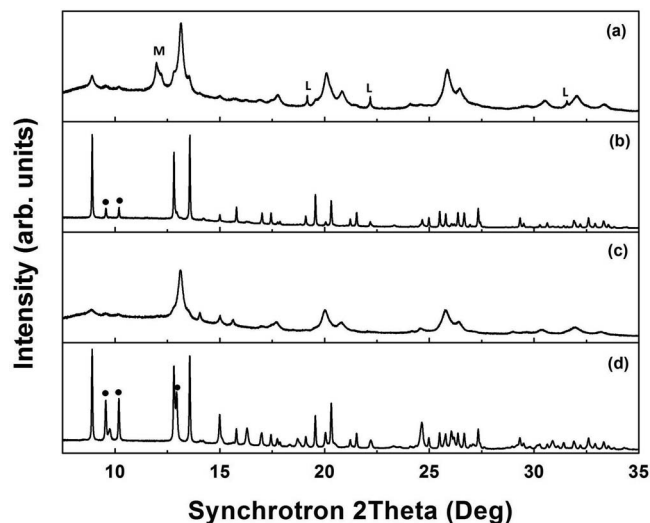


Figure 4. Alternating ball milling and heating cycles causes reversible phase transitions between the rutile and dirutile LiMnF_4 phases. XRD patterns are shown for (a) Rutile LiMnF_4 obtained by ball milling precursors LiF and MnF_3 . L and M denote the main peaks of unreacted LiF and MnF_3 precursor, respectively. (b) Dirutile LiMnF_4 obtained from heating sample A for 10 hours at 300°C under argon. Black circles denote the impurity Li_2MnF_5 phase. (c) Rutile LiMnF_4 obtained by ball milling sample B for 12 hours at 500 rpm. (d) Dirutile LiMnF_4 obtained from heating sample C for 10 hours at 300°C under argon. Black circles again denote the impurity Li_2MnF_5 phase. All XRD patterns were collected at Brookhaven National Laboratory NSLS, beamline x14A ($\lambda = 7.75756 \text{ \AA}$).

Results

Synthesis of dirutile LiMnF_4 .— Simply milling together LiF and MnF_3 in a planetary ball mill induces a mechanochemical reaction between the precursors, and a subsequent thermal treatment completes the reaction to dirutile LiMnF_4 . Figure 2a shows the XRD pattern collected after milling stoichiometric amounts of LiF and MnF_3 precursor for 6 hours at 500 rpm. While the main peaks of LiF and MnF_3 can still be seen, as marked by L and M, respectively, the primary peaks in this diffraction pattern belong to a new mechanochemically-formed rutile phase, which will be discussed in more detail in the Discussion section. Some dirutile LiMnF_4 has also formed mechanochemically.

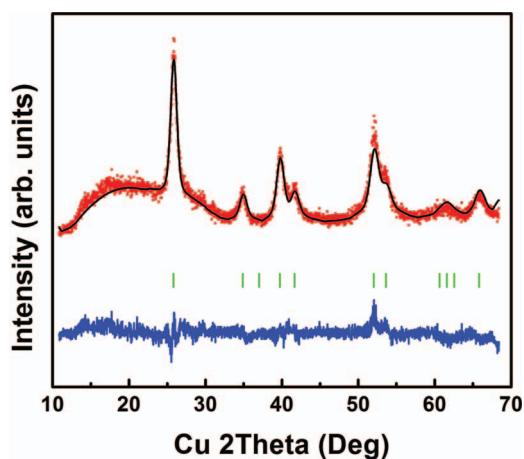


Figure 5. Rietveld refinement of the new rutile LiMnF_4 polymorph on the $\text{P4}_2/\text{mnm}$ space group shows good agreement between the experimental (red) and refined (black) diffraction patterns with $R_{wp} = 9.6\%$ and $\text{GOF} = 1.825$. The peak positions for rutile LiMnF_4 are shown by the green vertical lines, and the difference plot is shown by the bottom blue line.

The largest peaks of dirutile LiMnF_4 are found at 17.6° , 25.5° , and 27° $\text{Cu } 2\theta$, and can already be seen in Figure 2a after the first milling process.

Figure 2b, c, and d show the evolution of the reaction with increased firing temperatures. The rutile phase crystallizes at temperatures up to 250°C . Comparing the pattern from the milled precursors (Figure 2a) to the sample heated at 200°C (Figure 2b), we see that the intensity of the precursor peaks have decreased and the rutile peaks have sharpened, indicating the progression of the solid state reaction. The dirutile peaks grow as the sample is heated to higher temperatures. At 250°C (Figure 2c), the precursors have completely reacted, and the XRD pattern shows a partial transformation from the rutile phase to the dirutile LiMnF_4 phase. The dirutile peaks at 17.6° , 25.5° , and 27° $\text{Cu } 2\theta$ are significantly larger in Figure 2c than Figure 2b. Finally, at 300°C (Figure 2d), the rutile phase has completely disappeared, indicated by the missing rutile peak at 25.8° $\text{Cu } 2\theta$. The main peaks of Figure 2d match those of dirutile LiMnF_4 , and the two small impurity peaks denoted by black circles belong to Li_2MnF_5 . The impurity phase, Li_2MnF_5 , preferentially forms over dirutile LiMnF_4 when firing in air instead of argon. Further heating to temperatures between 300 – 600°C produces no changes in the obtained XRD patterns. Above 600°C , LiMnF_4 decomposes.

Adjusting the ratio of $\text{LiF}:\text{MnF}_3$ to include 10% excess MnF_3 eliminates the impurity Li_2MnF_5 phase after firing. Our refinement on the $\text{P2}_1/\text{c}$ space group for dirutile LiMnF_4 gives unit cell parameters of $a = 5.43 \text{ \AA}$, $b = 4.64 \text{ \AA}$, $c = 5.70 \text{ \AA}$, and $\beta = 113.18^\circ$ (Figure 3). These values are within 0.01 \AA and 0.1° of those reported by Wandner et al.²⁵

Synthesis of rutile LiMnF_4 .— Not only is a rutile phase dominant after mechanochemical reaction of LiF and MnF_3 , but this same rutile phase appears when ball milling dirutile LiMnF_4 by itself. In Figure 4, the reversibility of the phase transition between dirutile and rutile phases with ball milling and heating cycles is shown by distinct changes in the diffraction patterns. Figure 4a shows the diffraction pattern obtained after milling the precursors, where the main peaks in the pattern belong to a rutile phase and “L” and “M” denote the peaks of unreacted LiF and MnF_3 precursors. This sample is then heated under argon gas flow for 10 hours at 300°C , producing the crystalline dirutile phase in Figure 4b. Excluding the peaks marked by black circles, which belong to a Li_2MnF_5 impurity, all other peaks belong to dirutile LiMnF_4 . Milling the dirutile reverts it to rutile (Figure 4c), and reheating this rutile transforms it back to dirutile (Figure 4d).

Phase pure rutile LiMnF_4 is obtained after milling dirutile LiMnF_4 by itself for twelve hours. We could not match the peaks to any known phase, but noticed a similarity of the experimental diffraction pattern to that of rutile MnF_2 . Thus, we performed the Rietveld refinement using the $\text{P4}_2/\text{mnm}$ space group, assuming exactly half occupancy of the cation site by Li and Mn, as shown in Figure 5. The unit cell parameters of the new rutile phase are determined to be $a = b = 4.786 \text{ \AA}$ and $c = 2.985 \text{ \AA}$. We were unable to obtain a more crystalline sample of the new rutile phase for characterization. At just 300°C , the rutile transforms completely to the dirutile phase; lower temperatures also cause partial transformations.

Electrochemical performance of dirutile and rutile LiMnF_4 .— Three different LiMnF_4 samples were tested for electrochemical performance. Dirutile LiMnF_4 , obtained by solid state reaction, was ball milled with carbon for two hours before being made into electrodes. Rutile LiMnF_4 , obtained by ball milling dirutile LiMnF_4 by itself for twelve hours, was then ball milled with carbon for two hours. The last sample was obtained by ball milling dirutile LiMnF_4 for twelve hours with carbon. Dirutile LiMnF_4 partially transforms to rutile LiMnF_4 during the twelve hour milling cycle with carbon, and we will refer to these samples as the *two-phase* samples.

Figure 6a and b show the first cycle galvanostatic charge-discharge data of the dirutile and rutile samples, respectively. Cells were cycled at rates of C/20, C/50, and C/100. C/100 data is not shown in Figure 6

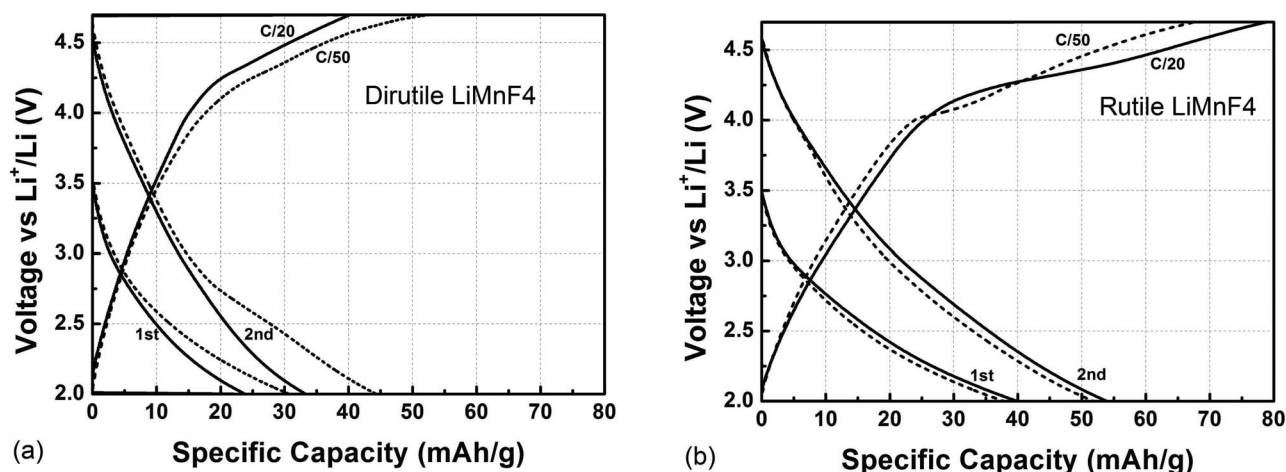


Figure 6. (a) First and second galvanostatic charge-discharge curves for dirutile LiMnF_4 milled for 2 hours with carbon at C/20 and C/50. (b) First and second galvanostatic charge-discharge curves for rutile LiMnF_4 milled for 2 hours with carbon at C/20 and C/50.

as the slower C/100 test rate shows no improvement in specific capacity over the C/50 test rate in either sample. In the second discharge, a specific capacity of 45 mAh/g was attained in the dirutile samples, and 55 mAh/g in the rutile samples. We hypothesize that the specific capacity of both these single-phase samples is low due to inadequate conductivity. The particle size distribution seen in TEM after milling with carbon is <30 nm for the rutile phase, and 100–200 nm for the dirutile phase (Supplementary Figure 1). Given the small particle sizes after milling and the high carbon content in the electrodes, a fraction of the capacity observed in samples may be due to capacitive storage in carbon.

Galvanostatic charge-discharge on the two-phase sample of dirutile and rutile LiMnF_4 was also performed at C/20, C/50, and C/100 rates (Figure 7). The C/100 sample reaches 170 mAh/g on first discharge, which is three times the capacities observed in single phase dirutile or rutile samples, and 92% of the theoretical capacity expected for a 1 Li reaction. For the two-phase samples tested at C/50 and C/20, the capacity of first discharge is 103 mAh/g and 84 mAh/g, respectively. The higher capacities of the two-phase sample are likely due to the longer milling time of active material with carbon, which reduces particle size and increases intermixing with carbon.

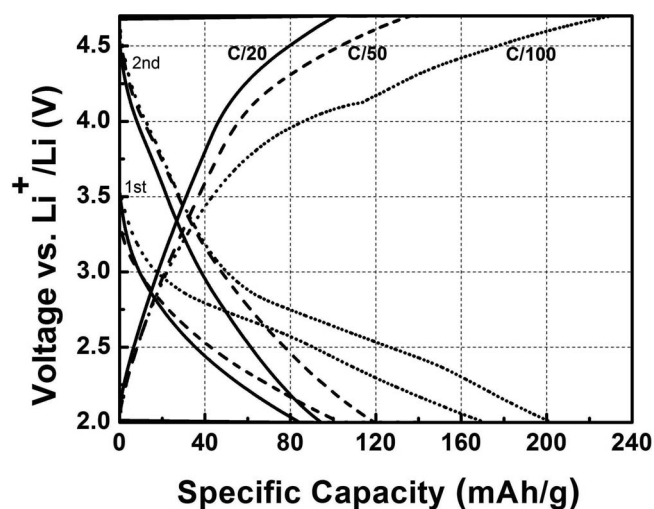


Figure 7. First and second galvanostatic charge-discharge curves for a two-phase sample of dirutile and rutile LiMnF_4 milled for 12 hours with carbon at C/20, C/50, and C/100.

Experimental confirmation of lithiation paths.— To distinguish between insertion and conversion of the LiMnF_4 phases upon lithiation, the rutile and dirutile samples were discharged at a C/100 rate to 3 V, 2 V, and 1 V and disassembled for ex situ TEM electron diffraction. Additionally, ex situ XRD patterns were collected on rutile and dirutile films discharged to 1 V before preparing the discharged films for TEM. The XRD showed LiMnF_4 peaks to be reduced in intensity but still present, and lattice parameters to be unchanged. Neither of the intercalated Li_2MnF_4 phases nor conversion products were detectable from XRD.

In contrast, distinct conversion products are visible in TEM for each of the three discharge levels of rutile LiMnF_4 . Figure 8 shows the SAED patterns obtained from rutile LiMnF_4 discharged to 3 V, 2 V, and 1 V. At the most shallow discharge level of 3 V, rutile LiMnF_4 phase is found most frequently in the indexed ring diffraction patterns (Figure 8a), but some of the rutile LiMnF_4 has been converted into LiF and MnF_2 . At the 2 V discharge level, most diffraction patterns show a superposition of the LiF and MnF_2 phases (Figure 8b). The LiF diffraction rings are much more diffuse than the MnF_2 ones at 2 V, which indicate LiF is poorly crystallized. Some rutile LiMnF_4 is still present at 2 V. At the 1 V discharge level, the indexed phases are α -Mn, MnF_2 , and LiF (Figure 8c). The intensity of the MnF_2 peaks is lower than those found in the 2 V sample, indicating that some MnF_2 is further reduced to α -Mn. For both the 2 V and 1 V samples, while there are still areas with unreacted rutile LiMnF_4 , we only show the SAED patterns from areas undergoing the obvious conversion reaction.

In contrast to the ring diffraction patterns observed in the rutile LiMnF_4 samples, dirutile LiMnF_4 spot diffraction patterns are observed at all levels of discharge (Figure 9a and b). The amorphous ring diffraction patterns of the conversion products, which are indexed to α -Mn metal, superimpose with the dirutile LiMnF_4 spot diffraction patterns. At 3 V, the α -Mn rings are observed occasionally, while by 1 V, the α -Mn rings are seen in all images. It was necessary to enhance the contrast or overexpose the dirutile pattern in order to observe the faint Mn amorphous rings. The difference in the diffraction patterns between rutile samples (ring pattern) and dirutile samples (spot pattern) is due to the different particle sizes from sample preparation: the particle sizes of dirutile LiMnF_4 prepared by solid state reaction were determined from TEM to be 100–200 nm, while rutile LiMnF_4 particles formed mechanochemically were <30 nm.

Calculated intercalation products.— Two compounds were computationally investigated as candidates for Li_2MnF_4 , the intercalation product of dirutile LiMnF_4 . The first structure, $\text{Li}_2\text{MnF}_4\text{-oct}$, was formed by inserting additional Li into the distorted octahedral voids in the lithium layer of dirutile LiMnF_4 , resulting in columns of

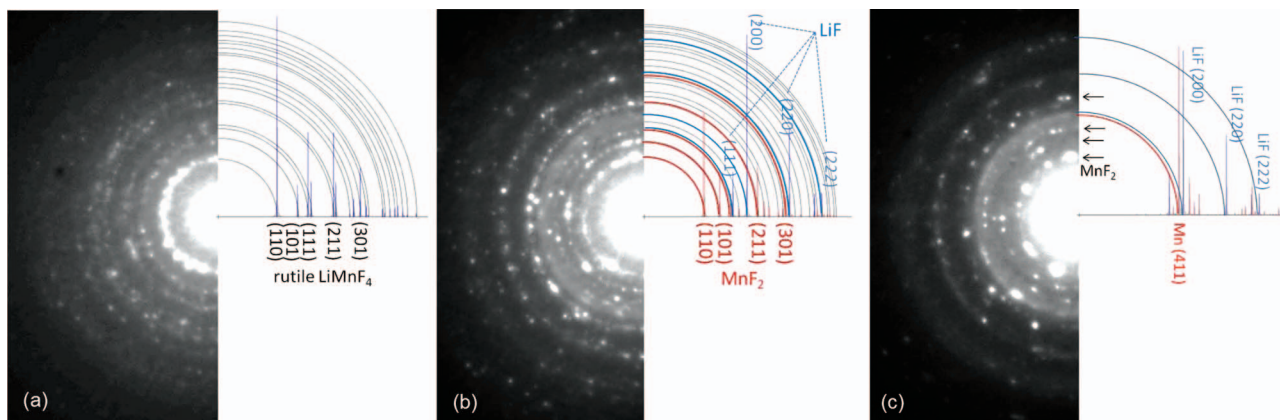


Figure 8. (a) The SAED pattern of rutile LiMnF_4 discharged to 3 V shows the rutile LiMnF_4 phase is still present in many regions of the sample. Rutile LiMnF_4 is the primary phase at this level of discharge, but some LiF and MnF_2 are also indexed in other SAED patterns, indicating the start of the conversion reaction. (b) The SAED pattern of rutile LiMnF_4 discharged to 2 V shows both the MnF_2 phase indexed by red peaks and amorphous LiF phase indexed by blue peaks in the same sample region. The diffused diffraction belt between LiF (111) and (200) indicates the presence of amorphous LiF converted from LiMnF_4 . (c) The SAED pattern of rutile LiMnF_4 discharged to 1 V shows the enhanced ring intensity corresponding to the Mn metal (411) peak indexed in red, and decreased intensity for MnF_2 peaks marked by the black arrows. The amorphous LiF phase is still present and is indexed by blue peaks.

face-sharing Li octahedra. The second structure, Li_2MnF_4 -tet, avoids Li octahedral face-sharing by splitting each octahedral Li site into two neighboring Li tetrahedral sites. The resultant Li_2MnF_4 -tet structure is topologically identical to La_2CuO_4 .²³ All calculations were initialized with monoclinic symmetry.

We determined lithium's preference for the tetrahedral sites by comparing energetics of the two possible Li_2MnF_4 intercalation products. Li_2MnF_4 -tet is preferred by a sizeable 97 meV/atom to Li_2MnF_4 -oct, corresponding to 339.5 meV/lithium. This is because lithium tetrahedra in Li_2MnF_4 -tet only edge-share with neighboring MnF_6 octahedra, while the lithium octahedra in Li_2MnF_4 -oct face-share with other lithium octahedra. The XRD patterns of Li_2MnF_4 -oct and Li_2MnF_4 -tet are clearly distinct from the dirutile LiMnF_4 or rutile LiMnF_4 patterns.

Additionally, two structures at intermediate lithiation levels between LiMnF_4 and Li_2MnF_4 were calculated. To gain insight into the dilute limit of insertion, $\text{Li}_{(1+x)}\text{MnF}_4$, a single octahedral Li was replaced by two tetrahedral Li in a $2 \times 2 \times 2$ supercell of LiMnF_4 , resulting in the composition $\text{Li}_{17/16}\text{MnF}_4$. Similarly, for the saturated limit, $\text{Li}_{(2-x)}\text{MnF}_4$, all but one octahedral lithium were replaced by two tetrahedral Li in the same $2 \times 2 \times 2$ supercell, resulting in composition $\text{Li}_{31/16}\text{MnF}_4$.

Figure 10 shows a possible structure of partially lithiated $\text{Li}_{(1+x)}\text{MnF}_4$, assuming some lithium intercalation into dirutile LiMnF_4 . MnF_6 octahedra are represented by the purple octahedra in the background, LiF_6 octahedra are represented by green octahedra

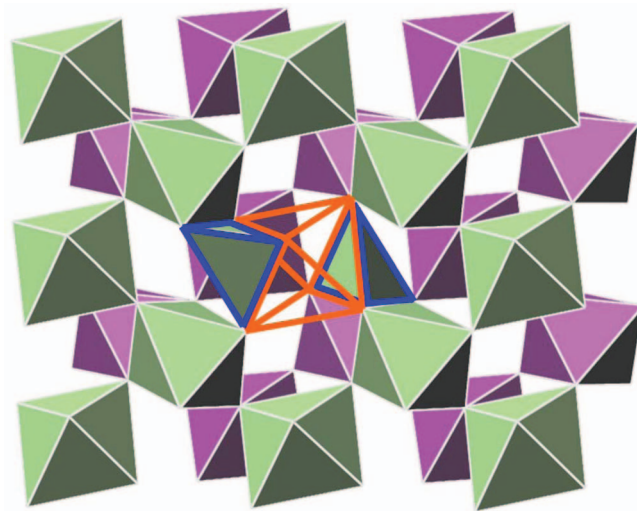


Figure 10. Lithium insertion into dirutile LiMnF_4 may induce a lithium site shift from the octahedral site (outlined in orange) to the two neighboring tetrahedral sites (outlined in blue). Partially lithiated $\text{Li}_{(1+x)}\text{MnF}_4$ is shown here with MnF_6 octahedra represented in purple in the background and LiF_6 octahedra represented in green in the foreground.

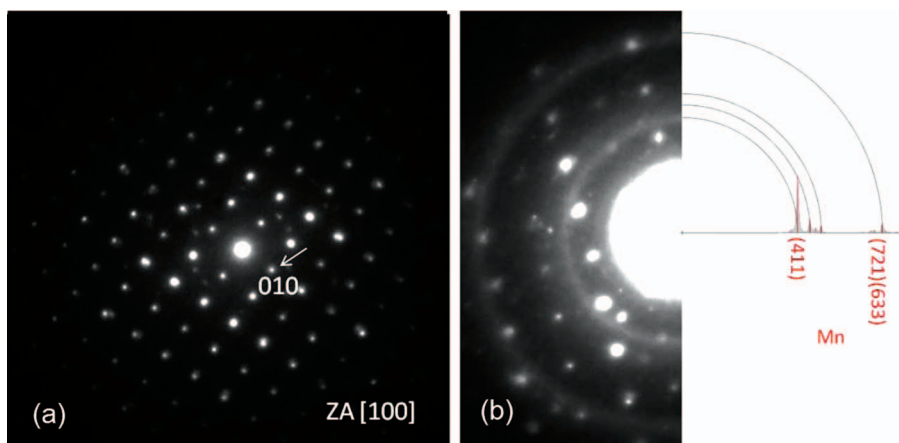


Figure 9. (a) The SAED patterns of dirutile LiMnF_4 discharged to 3 V mainly show a single crystal diffraction pattern indexed to dirutile LiMnF_4 , space group $P2_1/c$. Some patterns at 3 V show the superposition of faint α -Mn rings with the dirutile LiMnF_4 spot pattern. (b) The SAED patterns of dirutile LiMnF_4 discharged to 2 V and 1 V are indexed to the same phases. At 2 V, most patterns show superposition of α -Mn diffraction rings with the dirutile LiMnF_4 spot pattern, while at 1 V, α -Mn rings are observed with the LiMnF_4 spot pattern in all images.

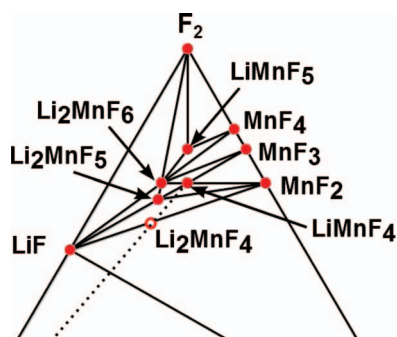
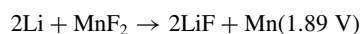
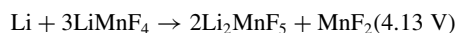


Figure 11. The Li-Mn-F phase diagram at 0 K is derived from first principles. Thermodynamically stable compounds are denoted by solid red dots. The lithiation path of LiMnF_4 is marked by the dotted line. Insertion into LiMnF_4 produces metastable Li_2MnF_4 , which is denoted by the open red dot.

in the foreground, and the original lithium octahedral site is outlined in orange. When an extra lithium ion enters the lithium layer, the original lithium shifts into one of the neighboring tetrahedral sites, and the extra lithium ion occupies the other tetrahedral site. The new lithium tetrahedral sites after intercalation are outlined in blue. These tetrahedral sites are face-sharing only with the original octahedral Li site and vertex-sharing with all other “non-split” Li octahedral sites.

Calculated reaction energies of conversion reactions.— Figure 11 shows the calculated Li-Mn-F equilibrium phase diagram at 0 K. Ground state compounds are denoted by the solid red dots. The two proposed structures for Li_2MnF_4 , the intercalation product of dirutile LiMnF_4 , are both metastable and marked by the open red dot on the phase diagram. From the phase diagram, the following equilibrium conversion reactions and voltages are expected with increasing lithium content:



The equilibrium conversion reactions are compared to possible non-equilibrium reaction paths in Figure 12. All compound energies are plotted relative to dirutile LiMnF_4 which sits at 0 meV per Li_xMnF_4 on the y-axis. At composition LiMnF_4 , the points in the range of 3–100 meV on the y-axis represent structures with alternative Li-Mn orderings. The other blue points at the top of Figure 12 show the energies of two intermediate insertion compounds ($\text{Li}_{17/16}\text{MnF}_4$ and $\text{Li}_{31/32}\text{MnF}_4$) and two fully intercalated compounds ($\text{Li}_2\text{MnF}_4\text{-oct}$ and $\text{Li}_2\text{MnF}_4\text{-tet}$). The computed energies for both intermediate compounds are higher in energy than the tie line between LiMnF_4 and $\text{Li}_2\text{MnF}_4\text{-tet}$, suggesting that if intercalation were to occur, it would take place as a two-phase insertion reaction directly from LiMnF_4 to $\text{Li}_2\text{MnF}_4\text{-tet}$ at 3.87 V.

The red points at the bottom of Figure 12 represent the equilibrium conversion products given by the phase diagram. While the equilibrium lithiation path traverses the $\text{Li}_2\text{MnF}_5 + \text{MnF}_2$ point before reaching $\text{LiF} + \text{MnF}_2$, converting dirutile LiMnF_4 directly to $\text{LiF} + \text{MnF}_2$ is not much higher in energy, and hence can occur with even modest underpotentials upon discharge.

The possible reaction paths are summarized in Figure 13. Boxes are placed top to bottom in order of increasing lithium chemical potential (lower voltage). Based on the experimental data, we assume lithium insertion occurs at most to a small extent (e.g. exclude Li_2MnF_4 -like phases). We also assume the metastable rutile phase is close in energy to dirutile LiMnF_4 , so that we have a single LiMnF_4 starting point at the top of the flow chart. Solid arrows connecting boxes denote likely reaction paths, while dashed arrows represent less plausible reaction paths which are shown only for the sake of completeness.

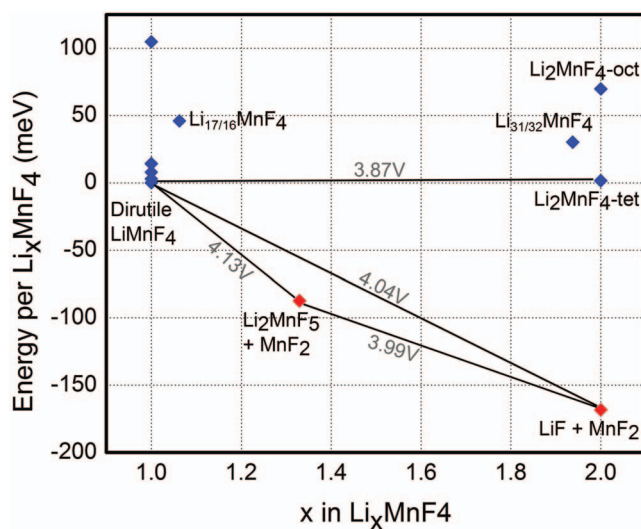


Figure 12. Energies of compositions between LiMnF_4 and Li_2MnF_4 are plotted relative to that of dirutile LiMnF_4 . Rutile polymorphs and insertion products ($\text{Li}_{1+x}\text{MnF}_4$) are represented by blue points, and competing conversion products at specific lithiation levels are represented by red points. Lines connecting points are labeled with the calculated equilibrium voltages between compounds. The equilibrium voltage is linearly related to the slope between points.

The numbers next to each arrow give the equilibrium reaction voltage between compounds in connected boxes.

Discussion

Synthesis of dirutile and rutile phases.— The reported synthesis methods of dirutile LiMnF_4 have the drawback of requiring a two-step process: fluorination of LiF and MnF_2 with fluorine gas to obtain an intermediate Mn^{4+} compound, which is then thermally decomposed to LiMnF_4 .^{25,26} We sought a direct, safe, and more environmentally friendly method of synthesizing LiMnF_4 , and found mechanochemistry followed by a low-temperature thermal treatment to be a successful alternative synthesis route. Our work adds to the recent trend in fluoride synthesis to utilize mechanochemistry rather than hydrofluoric acid or fluorine gas.^{27–30}

While mechanochemistry has been widely employed in recent years, the precise reaction mechanisms are still speculative, as they

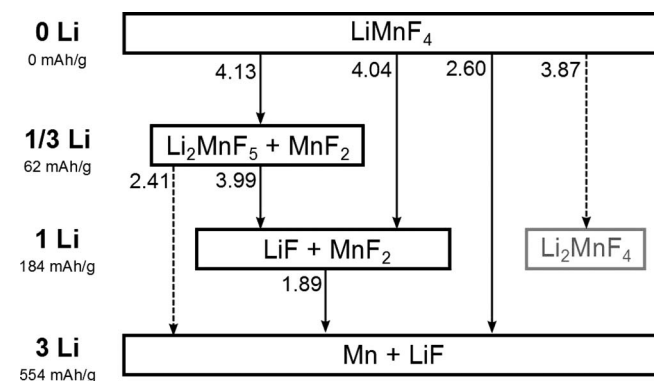


Figure 13. Starting with LiMnF_4 , possible reactions of fluoride compounds with lithium are labeled with their expected onset voltages. The lithium fraction and specific capacity listed to the left of each box are calculated relative to LiMnF_4 . Less plausible reactions are denoted by dashed arrows, while more plausible reactions are denoted by solid arrows. The gray box containing Li_2MnF_4 assumes insertion and lithium site shift. All other boxes represent conversion products from reactions with lithium.

are hard to evaluate either experimentally or computationally.³¹ The cause of mechanically-induced phase transitions in certain materials is also not well understood - they may occur as a combined result of shear, high defect concentration, and high temperatures.³²⁻³⁵ The dirutile-to-rutile phase transformation observed in our work follows similar trends seen in other oxides and fluorides. Short milling times can produce polymorphs that are metastable at ambient temperature and pressure. These metastable phases tend to be the equilibrium phases at high pressure and/or high temperature conditions, and have more compact structures.³² The mechanically-formed rutile LiMnF_4 follows this behavior with a smaller volume than its dirutile counterpart, 68 \AA^2 vs. 71 \AA^2 per formula unit. It is unclear if the new rutile polymorph of LiMnF_4 forms because of the extreme processing conditions seen in the ball mill or because of stabilizing surface energy effects at the nanoscale.

Plausibility and stability of the new rutile LiMnF_4 phase.— While mechanically-induced phase transformations are difficult to model, computations can still be used to investigate the stability of the final rutile LiMnF_4 polymorph. Rietveld refinement suggests that rutile LiMnF_4 is disordered on the cation site with equal probability of occupation of the site by Li or Mn. To estimate the energy scale of cation disorder in the rutile framework, thirteen symmetrically-distinct structures with alternate Li-Mn orderings were calculated with a unit cell of less than or equal to 18 atoms. Six of the thirteen structures were within 31 meV/atom of the ground state dirutile LiMnF_4 , and four were within 5 meV/atom. While these alternative orderings are not identical to the disordered structure used in Rietveld refinement, the small energetic difference between Li-Mn orderings in LiMnF_4 is consistent with a phase which would show Li-Mn disorder. This agrees with experimental observations where simple mechanical milling causes a phase transition from the ordered dirutile to disordered rutile LiMnF_4 , and the reverse reaction is activated by thermal treatment.

Conversion reaction paths of LiMnF_4 .— As shown by galvanostatic charge-discharge tests and ex situ TEM electron diffraction, rutile and dirutile LiMnF_4 are both electrochemically active but convert upon lithiation along different reaction paths. The observed reactions do not match the equilibrium conversion reactions given by the phase diagram. This may either be an artifact of TEM performed ex situ rather than in situ and not all intermediate reactions being captured, or because rutile and dirutile LiMnF_4 simply convert via nonequilibrium reaction paths upon lithiation. All reactions are summarized graphically in Figure 13.

In the equilibrium reaction, the first expected reaction upon lithiation is the conversion of LiMnF_4 to Li_2MnF_5 and MnF_2 at 4.13 V, followed by the conversion of Li_2MnF_5 to MnF_2 and LiF at 3.99 V. However, in the SAED patterns of discharged rutile samples, neither Li_2MnF_5 nor superpositioned Li_2MnF_5 and MnF_2 patterns are observed. The first observed conversion products are MnF_2 and LiF , which first appear alongside rutile LiMnF_4 at the 3 V discharge level. These observations suggest that either the Li_2MnF_5 formed at 4.13 V quickly decomposes into MnF_2 and LiF at 3.99 V, or rutile LiMnF_4 converts directly to LiF and MnF_2 at 4.04 V.

If we assume that rutile LiMnF_4 follows the center 4.04 V path in Figure 13 ($\text{LiMnF}_4 \rightarrow \text{LiF} + \text{MnF}_2$), the subsequent conversion to Mn and LiF is not expected to begin until 1.89 V. Our experimental results agree well with theory: at 2 V, MnF_2 and LiF are the dominant phases. Some rutile LiMnF_4 is also still observed, but Mn metal is not. The presence of some rutile LiMnF_4 in the 2 V sample suggests that the direct conversion of rutile LiMnF_4 to Mn metal is not preferred. As seen in Figure 13, the direct reaction of $\text{LiMnF}_4 \rightarrow \text{Mn} + \text{LiF}$ is predicted to begin at 2.60 V. If this 2.60 V reaction path were active, we would expect to see some Mn metal in the 2 V sample.

The rutile sample further discharged to 1 V is indexed to $\alpha\text{-Mn}$, LiF , and some remnant MnF_2 . Rutile LiMnF_4 is no longer observed at 1 V. Between 2 V and 1 V, rutile LiMnF_4 may either convert directly to $\text{LiF} + \text{Mn}$, or form MnF_2 before converting to $\text{LiF} + \text{Mn}$. The MnF_2 peaks in the 1 V sample are weaker than those in the 2 V sample,

suggesting there is less MnF_2 present in the sample at 1 V because of the further conversion to $\alpha\text{-Mn}$. The diffused ring patterns of the converted LiF and Mn metal phases show that they are much smaller in particle size than the starting phase of rutile LiMnF_4 , which is typical of conversion products in battery cathodes. It is clear that rutile LiMnF_4 is converting, but we cannot entirely rule out the possibility of lithium insertion at the start of discharge, where the discharge specific capacity may have contributions from both insertion and conversion reactions. A small amount of lithium insertion may be possible if conversion of LiMnF_4 is kinetically limited.

In contrast to the ring patterns observed in the rutile samples, dirutile LiMnF_4 samples discharged between 3 V and 1 V all show a component of single crystal spot diffraction patterns (Figure 9a and b) which belong to 100–200 nm dirutile LiMnF_4 particles. The superimposed amorphous ring patterns are from the conversion product, $\alpha\text{-Mn}$, formed during discharge. This is the only conversion product indexed in the discharged dirutile LiMnF_4 samples. $\alpha\text{-Mn}$'s unexpected appearance at the 3 V discharge level suggests that lithiation of dirutile LiMnF_4 is dominated by direct conversion to $\text{LiF} + \text{Mn}$. It is not yet determined why $\alpha\text{-Mn}$ is seen at 3 V when the conversion of $\text{LiMnF}_4 \rightarrow \text{Mn} + \text{LiF}$ is predicted to begin at 2.60 V. LiF is not observable in the SAED patterns because it is a weaker scatterer than Mn. Like rutile LiMnF_4 , dirutile LiMnF_4 is clearly converting to LiF and Mn, but may also be inserting at the start of discharge.

Although the possibility of electron beam damage cannot be excluded as an explanation for $\alpha\text{-Mn}$'s presence in the 3 V discharged sample, $\alpha\text{-Mn}$'s amorphous ring pattern is only observed in several SAED patterns out of the 30 measured patterns taken from different areas of the TEM sample. In contrast, in the 2 V and 1 V discharged samples, $\alpha\text{-Mn}$ is observed in most SAED patterns. Considering the measurement condition for SAED is kept constant for all measurements with the broadest electron beam, this difference observed by SAED is most likely not an artifact. Using scanning TEM techniques including STEM, we found that STEM as a focused beam technique caused obvious artifacts and beam damage to these fluorides compared with the conventional TEM technique of SAED.

Finally, we consider the remaining reaction paths shown in Figure 13. The reaction at 2.41 V converting Li_2MnF_5 and MnF_2 directly to LiF and Mn is unlikely; if this reaction path were active, Li_2MnF_5 should have been observed in a 3 V sample. Thus, the 2.41 V reaction is labeled with a dashed arrow to denote a less plausible reaction. Insertion to Li_2MnF_4 at 3.89 V is also unlikely - no evidence of insertion is seen in XRD or TEM, and thermodynamically, conversion is preferred over insertion (Figure 12).

Optimization of electrochemical performance.— One of the open questions from our work is how to improve the specific capacity in a single phase of LiMnF_4 . Only short milling times were used to mix the active cathode material with carbon in order to maintain single-phase samples. However, higher capacities were observed in two-phase samples attained by extending the milling times of the cathode material with carbon. A twelve hour milling cycle of dirutile LiMnF_4 with carbon transformed the sample to a two phase mixture of dirutile and rutile LiMnF_4 with particle sizes of <30 nm. As shown in Figure 7, this two-phase sample achieved a capacity of 170 mAh/g upon first discharge and cycled reversibly. With a twelve hour milling cycle of rutile LiMnF_4 with carbon, we observed a transformation of the active material to LiF and MnF_2 . These are the same conversion intermediates observed in discharged samples of rutile LiMnF_4 , but the two-phase sample starting with LiF and MnF_2 showed an increase in specific capacity from 40 mAh/g to 100 mAh/g on first discharge. As with other fluoride materials, we believe the key to realizing higher capacities is reducing particle sizes and achieving good intermixing with a conductive matrix. For the LiMnF_4 polymorphs, this is a problem as they are not stable under long milling times with carbon. Other synthesis and electrode preparation methods may have more success in achieving small particle sizes in a single phase LiMnF_4 to reach its theoretical conversion capacity of 584 mAh/g.

Conclusions

Dirutile LiMnF_4 was computationally identified to be a promising new conversion cathode material for lithium-ion batteries. In this work, two polymorphs of LiMnF_4 were synthesized, tested as lithium-ion battery cathodes, and studied using electron diffraction and computation to understand their lithiation mechanisms. Synthesis of dirutile LiMnF_4 , a known compound, was achieved by a new low-temperature mechanochemical/solid state reaction route, and the new rutile polymorph of LiMnF_4 was synthesized by mechanical milling. Both phases were shown to be electrochemically active, but took different non-equilibrium reaction paths upon lithiation. Dirutile LiMnF_4 converts directly to LiF and Mn , while rutile samples forms MnF_2 before converting to LiF and Mn metal. Computations suggest that the two nonequilibrium paths taken by the samples are close in energy to the ground state path.

Due to lack of stability under long ball milling, phase-pure samples of dirutile and rutile cannot be well mixed with carbon or reduced in particle size, leading to low specific capacities. Two-phase samples of dirutile and rutile LiMnF_4 , which were derived from longer milling times, showed substantially larger capacity. Hence, these results identify an opportunity for improving capacity if alternative sample and electrode preparation methods are found to obtain smaller particle size and better carbon-mixed electrodes.

Acknowledgments

This work was supported by Robert Bosch Corporation and Umicore Specialty Oxides and Chemicals, as well as the National Science Foundation Graduate Research Fellowship under Grant # 1122374. Powder diffraction patterns in Figure 4 were collected at Brookhaven National Laboratory NSLS (Beamline x14A). This work also made use of the MRSEC Shared Experimental Facilities at MIT, supported by the National Science Foundation under award # DMR-08-19762. We acknowledge support from the National Science Foundation through TeraGrid resources provided by Texas Advanced Computing Center (TACC) under grant number TG-DMR970008S.

References

- I. Plitz, F. Badway, J. F. Al-Sharab, A. DuPasquier, F. Cosandey, and G. G. Amatucci, *Journal of The Electrochemical Society*, **152**, A307 (2005).
- F. Badway, F. Cosandey, N. Pereira, and G. G. Amatucci, *Journal of The Electrochemical Society*, **150**, A1318 (2003).
- M. Bervas, A. N. Mansour, W. S. Yoon, J. F. Al-Sharab, F. Badway, F. Cosandey, L. C. Klein, and G. G. Amatucci, *Journal of The Electrochemical Society*, **153**, A799 (2006).
- H. Arai, S. Okada, Y. Sakurai, and J. Yamaki, *Journal of Power Sources*, **68**, 716 (1997).
- F. Badway, N. Pereira, F. Cosandey, and G. G. Amatucci, *Journal of The Electrochemical Society*, **150**, A1209 (2003).
- N. Pereira, F. Badway, M. Wartelsky, S. Gunn, and G. G. Amatucci, *Journal of The Electrochemical Society*, **156**, A407 (2009).
- F. Wang, R. Robert, N. A. Chernova, N. Pereira, F. Omenya, F. Badway, X. Hua, M. Ruotolo, R. Zhang, L. Wu, V. Volkov, D. Su, B. Key, M. S. Whittingham, C. P. Grey, G. G. Amatucci, Y. Zhu, and J. Graetz, *Journal of the American Chemical Society*, **133**, 18828 (2011).
- F. Wang, H. C. Yu, M. H. Chen, L. Wu, N. Pereira, K. Thornton, A. Van der Ven, Y. Zhu, G. G. Amatucci, and J. Graetz, *Nature Communications*, **3**, 1201 (2012).
- V. L. Chevrier, G. Hautier, S. P. Ong, R. E. Doe, and G. Ceder, *Physical Review B*, **87**, 094118 (2013).
- K. M. Wiaderek, O. J. Borkiewicz, E. Castillo-Martínez, R. Robert, N. Pereira, G. G. Amatucci, C. P. Grey, P. J. Chupas, and K. W. Chapman, *Journal of the American Chemical Society*, **135**, 4070 (2013).
- F. Badway, A. N. Mansour, N. Pereira, J. F. Al-Sharab, F. Cosandey, I. Plitz, and G. G. Amatucci, *Chemistry of Materials*, **19**, 4129 (2007).
- R. E. Doe, K. A. Persson, G. Hautier, and G. Ceder, *Electrochemical and Solid-State Letters*, **12**, A125 (2009).
- S. W. Kim, D. H. Seo, H. Gwon, J. Kim, and K. Kang, *Advanced Materials*, **22**, 5260 (2010).
- R. E. Doe, K. A. Persson, Y. S. Meng, and G. Ceder, *Chemistry of Materials*, **20**, 5274 (2008).
- A.-L. Dalverny, J.-S. Filhol, and M.-L. Doublet, *Journal of Materials Chemistry*, **21**, 10134 (2011).
- A. Jain, G. Hautier, C. J. Moore, B. Kang, J. Lee, H. Chen, N. Twu, and G. Ceder, *Journal of The Electrochemical Society*, **159**, A622 (2012).
- H. Chen, G. Hautier, and G. Ceder, *Journal of the American Chemical Society*, **134**, 19619 (2012).
- P. Lacorre, J. Pannetier, F. Averdunk, R. Hoppe, and G. Ferrey, *Journal of Solid State Chemistry*, **79**, 1 (1989).
- A. Jain, G. Hautier, C. J. Moore, S. P. Ong, C. C. Fischer, T. Mueller, K. A. Persson, and G. Ceder, *Computational Materials Science*, **50**, 2295 (2011).
- J. Perdew, K. Burke, and M. Ernzerhof, *Physical Review Letters*, **77**, 3865 (1996).
- V. I. Anisimov, J. Zaanen, and O. K. Andersen, *Physical Review B*, **44**, 943 (1991).
- www.materialsproject.org.
- C. Chaillout and M. Mazzeo, in *Materials and Crystallographic Aspects of HTE-Superconductivity*, **263**, 129 (1994).
- M. Bervas, L. C. Klein, and G. G. Amatucci, *Journal of The Electrochemical Society*, **153**, A159 (2006).
- K. H. Wandner and R. Hoppe, *Zeitschrift für anorganische und allgemeine Chemie*, **546**, 113 (1987).
- R. Hoppe, W. Dähne, and W. Klemm, *Justus Liebigs Annalen der Chemie*, **658**, 1 (1962).
- I. Gocheva, M. Nishijima, T. Doi, S. Okada, J. Yamaki, and T. Nishida, *Journal of Power Sources*, **187**, 247 (2009).
- R. A. Shaloor, S. Yeon, H. Kim, K. Nam, J. Ku, K. Kang, and J. Wook, *Solid State Ionics*, **218**, 35 (2012).
- W. Tong and G. G. Amatucci, *Journal of Power Sources*, **196**, 1449 (2011).
- I. Gocheva, K. Chihara, S. Okada, and J. Yamaki, *LiBD-5* (2011).
- S. James, C. J. Adams, C. Bolm, D. Braga, P. Collier, T. Friščić, F. Grepioni, K. D. M. Harris, G. Hyett, W. Jones, A. Krebs, J. Mack, L. Maini, A. G. Orpen, I. P. Parkin, W. C. Shearouse, J. W. Steed, and D. C. Waddell, *Chem Soc Rev*, **41**, 413 (2011).
- V. Sepelák, S. Bégin-Colin, and G. Le Caër, *Dalton Transactions*, **41**, 11927 (2012).
- M. Bervas, F. Badway, L. C. Klein, and G. G. Amatucci, *Electrochemical and Solid-State Letters*, **8**, A179 (2005).
- Y. Wu, Y. Zhang, G. Pezzotti, and J. Guo, *Materials Letters*, **52**, 366 (2002).
- G. Dénès, D. Le Roux, and M. C. Madamba, *Materials Research Society Symposium Proceedings*, **481**, 667 (1998).